

Coherence of temperature and velocity superstructures in turbulent Rayleigh-Bénard flow

Dominik Krug^{1†}, Detlef Lohse^{1,2}, and Richard J.A.M. Stevens¹

¹Physics of Fluids Group and Twente Max Planck Center, Department of Science and Technology, Mesa+ Institute, and J.M. Burgers Center for Fluid Dynamics, University of Twente, P.O. Box 217, 7500 AE Enschede, The Netherlands

²Max Planck Institute for Dynamics and Self-Organization, Am Fassberg 17, 37077 Göttingen, Germany

(Received xx; revised xx; accepted xx)

We investigate the interplay between large-scale patterns, so-called superstructures, in the fluctuation fields of temperature θ and vertical velocity w in turbulent Rayleigh-Bénard convection at large aspect ratios. Earlier studies suggested that velocity superstructures were smaller than their thermal counterparts in the center of the domain. However, a scale-by-scale analysis of the correlation between the two fields employing the linear coherence spectrum reveals that superstructures of the same size exist in both fields, which are almost perfectly correlated. The issue is further clarified by the observation that in contrast to the temperature, and unlike assumed previously, superstructures in the vertical velocity field do not result in a peak in the power spectrum of w . The origin of this difference is traced back to the production terms of the θ - and w -variance. These results are confirmed for a range of Rayleigh numbers $Ra = 10^5$ – 10^9 , the superstructure size is seen to increase monotonically with Ra . It is further observed that the scale distribution of particularly the temperature fluctuations is pronouncedly bimodal. In addition to the large-scale peak caused by the superstructures, there exists a strong small-scale peak. This ‘inner peak’ is most intense at a distance of δ_θ off the wall and associated with structures of size $\approx 10\delta_\theta$, where δ_θ is the thermal boundary layer thickness. Finally, based on the vertical coherence with reference height of δ_θ , a self-similar structure is identified in the velocity field (vertical and horizontal components) but not in the temperature.

Key words:

1. Introduction

A remarkable feature of turbulent flows is that amid the inherent disorder both in time and space, they frequently give rise to a surprisingly organized flow motion on very large scales. Such very large-scale structures in the fully turbulent regime have, for example, been reported for turbulent boundary layers (Hutchins & Marusic 2007a), plane Couette flow (Lee & Moser 2018), and Taylor-Couette (Huisman *et al.* 2014) turbulence. Here we focus on superstructures in turbulent Rayleigh-Bénard convection (RBC), which is an idealized configuration that is widely used to study thermal convection (Ahlers *et al.*

† Email address for correspondence: d.j.krug@utwente.nl

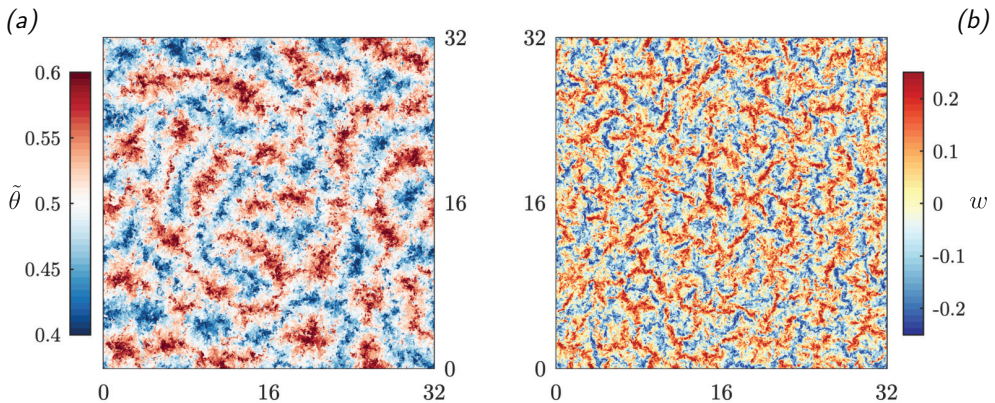


FIGURE 1. Snapshots of the temperature (a) and the vertical velocity (b) field at mid-height for a simulation in a $\Gamma = 32$ cell with $Pr = 1$ at $Ra = 10^8$.

2009; Lohse & Xia 2010; Chillà & Schumacher 2012). The strength of the non-dimensional thermal driving in RBC is given by the Rayleigh number Ra , while the dimensionless heat transfer is characterized by the Nusselt number Nu .

Large-scale organization in convective flows is widespread. An astonishing example is the formation of so-called cloud streets in the atmosphere that can extend for hundreds of kilometers (e.g. Young *et al.* 2002). Studying related features in RBC requires a cell with a large aspect ratio Γ . Naturally, this poses a challenge to experiments and simulations. Experimentally (e.g. Fitzjarrald 1976; Sun *et al.* 2005*a,b*; Zhou *et al.* 2012; Hogg & Ahlers 2013; Du Puits *et al.* 2013; Cierpka *et al.* 2019), it is very challenging to extract flow information beyond global parameters or local measurements of turbulence statistics. On the other hand, simulations for large aspect ratios are very costly if the thermal driving is sufficiently strong to achieve a moderately or even a strongly turbulent state. The first to tackle the problem numerically were Hartlep *et al.* (2003) and several related studies have since been presented in the literature (Parodi *et al.* 2004; Hartlep *et al.* 2005; Shishkina & Wagner 2005, 2006, 2007; Von Hardenberg *et al.* 2008; Bailon-Cuba *et al.* 2010; Emran & Schumacher 2015; Sakievich *et al.* 2016). Very recently, the available ranges of large-aspect ratio simulations have been extended significantly in Prandtl number (Pr) by Pandey *et al.* (2018) and in Γ as well as in Ra by Stevens *et al.* (2018).

From these papers, it has become clear that in RBC superstructures, i.e., flow structures that are significantly larger than the convection rolls at onset (see, e.g. Drazin & Reid 2004) or in the weakly non-linear regime (Morris *et al.* 1993), exist at higher Ra . It is widely observed that the superstructure size increases with Ra (Fitzjarrald 1976; Hartlep *et al.* 2003; Pandey *et al.* 2018; Green *et al.* 2019), while the Pr -dependence appears to be more complicated. For the latter, Pandey *et al.* (2018) report that at $Ra = 10^5$ the largest structures are found for $Pr \approx 7$, but Pr -variations over a significant range at higher Ra have not been reported yet. Stevens *et al.* (2018) showed that very large domain sizes up to $\Gamma = 64$ are necessary to fully converge the size of the superstructures at $Ra = 10^8$. Finally, Von Hardenberg *et al.* (2008) and Pandey *et al.* (2018) demonstrate that superstructures evolve on timescales much longer than the free-fall time scale.

There is no consensus yet on how to best extract and quantify the superstructures in RBC. Researchers have relied on peaks in velocity and/or temperature power spectra (Von Hardenberg *et al.* 2008; Pandey *et al.* 2018; Stevens *et al.* 2018), velocity-

Ra	$N_x \times N_y \times N_z$	Nu	Re_h	Re_v	Re_t	\hat{l}
1×10^5	$2048 \times 2048 \times 64$	4.35	55.7	40.3	68.7	4.4
4×10^5	$2048 \times 2048 \times 64$	6.48	111.7	84.3	140.0	4.5
1×10^6	$3072 \times 3072 \times 96$	8.34	176.0	131.6	219.8	4.9
4×10^6	$3072 \times 3072 \times 96$	12.27	349.7	250.8	430.4	5.4
1×10^7	$4096 \times 4096 \times 128$	15.85	547.1	380.1	666.2	5.9
1×10^8	$6144 \times 6144 \times 192$	30.94	1660.3	1056.1	1967.8	6.3
1×10^9	$12288 \times 12288 \times 384$	61.83	4879.2	2962.3	5708.1	6.6

TABLE 1. The columns from left to right indicate the Ra number, the numerical resolution in the horizontal and wall normal directions ($N_x \times N_y \times N_z$), the Nu number, and the horizontal (Re_h), vertical (Re_v), and total (Re_t) Reynolds numbers. The length scale \hat{l} denotes the superstructure scale based on the coherence spectrum $\gamma_{\theta w}^2$ (plotted as triangles in figure 8b).

temperature co-spectra (Hartlep *et al.* 2003; Green *et al.* 2019; Fitzjarrald 1976) or so-called integral length scales (Parodi *et al.* 2004; Stevens *et al.* 2018) to determine the structure size. A puzzling and yet unexplained observation is that superstructures in the temperature (θ) field are larger than in the vertical velocity w (Pandey *et al.* 2018; Stevens *et al.* 2018) field when the structure size is determined based on the peaks in the power spectrum or the corresponding integral length scale. Also visually, the difference between the temperature and vertical velocity fields can easily be observed in the snapshots of the flow at mid-height, which are presented in figure 1. This figure reveals that the vertical velocity field is dominated by significantly smaller structures than the temperature field. Moreover, the correlation between the two quantities appears much lower than one would naively expect, given that the temperature fluctuations provide the driving of w . These observations seem at odds with the notion that superstructures in RBC form large-scale convection rolls for which temperature and velocity scales should be of the same size.

To address and clarify this issue along with related questions, we use the dataset of Stevens *et al.* (2018) to assess energy distributions and coherence on a scale-by-scale basis. Before presenting our results in §3, we provide the relevant details on the dataset of Stevens *et al.* (2018), together with the parameters of additional simulations performed for this study, in §2. We summarize our findings in §4.

2. Dataset

We solve the Boussinesq equations with the second-order staggered finite difference code AFiD. The code has been extensively validated and details of the numerical methods can be found in Verzicco & Orlandi (1996); Stevens *et al.* (2010, 2011); van der Poel *et al.* (2015); Zhu *et al.* (2018). The governing equations in dimensionless form read:

$$\frac{\partial \mathbf{u}}{\partial t} + \mathbf{u} \cdot \nabla \mathbf{u} = -\nabla p + \sqrt{\frac{Pr}{Ra}} \nabla^2 \mathbf{u} + \theta \hat{z}, \quad (2.1)$$

$$\nabla \cdot \mathbf{u} = 0, \quad (2.2)$$

$$\frac{\partial \theta}{\partial t} + \mathbf{u} \cdot \nabla \theta = \frac{1}{\sqrt{RaPr}} \nabla^2 \theta, \quad (2.3)$$

where \hat{z} is the unit vector pointing in the opposite direction of gravity, \mathbf{u} the velocity vector normalized by the free fall velocity $\sqrt{g\alpha\Delta H}$, t the dimensionless time normalized

by $\sqrt{H/(g\alpha\Delta)}$, θ the temperature normalized by Δ , and p the pressure normalized by $g\alpha\Delta/H$. The control parameters of the system are $Ra = \alpha g \Delta H^3 / (\nu \kappa)$ and $Pr = \nu / \kappa$, where α is the thermal expansion coefficient, g the gravitational acceleration, Δ the temperature drop across the container, H the height of the fluid domain, ν the kinematic viscosity, and κ the thermal diffusivity of the fluid. The boundary conditions on the top and bottom plates are no-slip for the velocity and constant for the temperature. Periodic conditions in the horizontal directions are used. In all our simulations, Pr is fixed to 1 and we analyze data for $\Gamma = L/H = 32$, where H is the vertical distance between the plates and L the horizontal extension of the domain. Coordinates in the wall-parallel direction are denoted by x and y while the z -axis points along the wall-normal. Horizontal velocity components are denoted v_x and v_y , respectively. A high spatial resolution in the boundary layer and bulk has been used to ensure that the resolution criteria set by Stevens *et al.* (2010) and Shishkina *et al.* (2010) are fulfilled. Details about the simulations can be found in table 1. The simulations for $Ra = 10^8$ and $Ra = 10^9$ have been reported before in Stevens *et al.* (2018), while the simulations for $10^5 \leq Ra \leq 10^7$ have been performed for this study. The horizontal, vertical, and total Reynolds numbers indicated in table 1 represent the volume and time averaged integrals of $\sqrt{(v_x^2 + v_y^2)}$, $\sqrt{(w^2)}$, and $\sqrt{(v_x^2 + v_y^2 + w^2)}$, respectively. In the following, we decompose instantaneous quantities $\tilde{\psi}$ into mean and fluctuating parts according to $\tilde{\psi} = \Psi + \psi$, where $\Psi = \langle \tilde{\psi} \rangle$ with $\langle \cdot \rangle$ denoting an average over a wall-parallel plane and time.

3. Results

In presenting our results, we initially (§3.1–§3.3) restrict the discussion to a single Rayleigh number ($Ra = 10^8$). A detailed discussion of the Ra -dependence of our findings is then provided in §3.4.

3.1. Spectral distribution of energy and coherence of temperature and vertical velocity

To evaluate the energy distribution across different scales, we first consider the one-sided power spectra $\Phi_{\psi\psi}(k)$, where ψ is a zero-mean quantity (velocity or temperature here) and k is the radial wavenumber $k = \sqrt{k_x^2 + k_y^2}$. The spectra are computed for horizontal planes and averaged in time. Results for θ and w at several distances from the wall are presented in figures 2a and 2b, respectively. Data are presented in premultiplied form $k\Phi_{\psi\psi}$, such that the area under the curve equals the variance when plotted on a logarithmic scale, according to

$$\langle \psi^2 \rangle = \int_0^\infty \Phi_{\psi\psi} dk = \int_0^\infty k \Phi_{\psi\psi} d(\log k). \quad (3.1)$$

For reference, the wall-normal temperature and vertical velocity variance profiles are presented in figures 3a and 3b, respectively. The symbols in these figures mark the positions at which the spectra in figure 2 are computed.

First, we focus on the situation at mid-height ($z/H = 0.5$), which corresponds to the location of the snapshots shown in figure 1. These results are represented by the red lines in figure 2. Figure 2a shows that the temperature spectrum $k\Phi_{\theta\theta}(z/H = 0.5)$ has a pronounced peak in the range $k \approx 1 \pm 0.4$ that corresponds to the superstructures. This peak contains about half of the temperature variance at $z/H = 0.5$, while the remainder of the variance is spread out over a wide range of intermediate and small-scales which individually carry relatively little energy. Figure 2b reveals that the corresponding

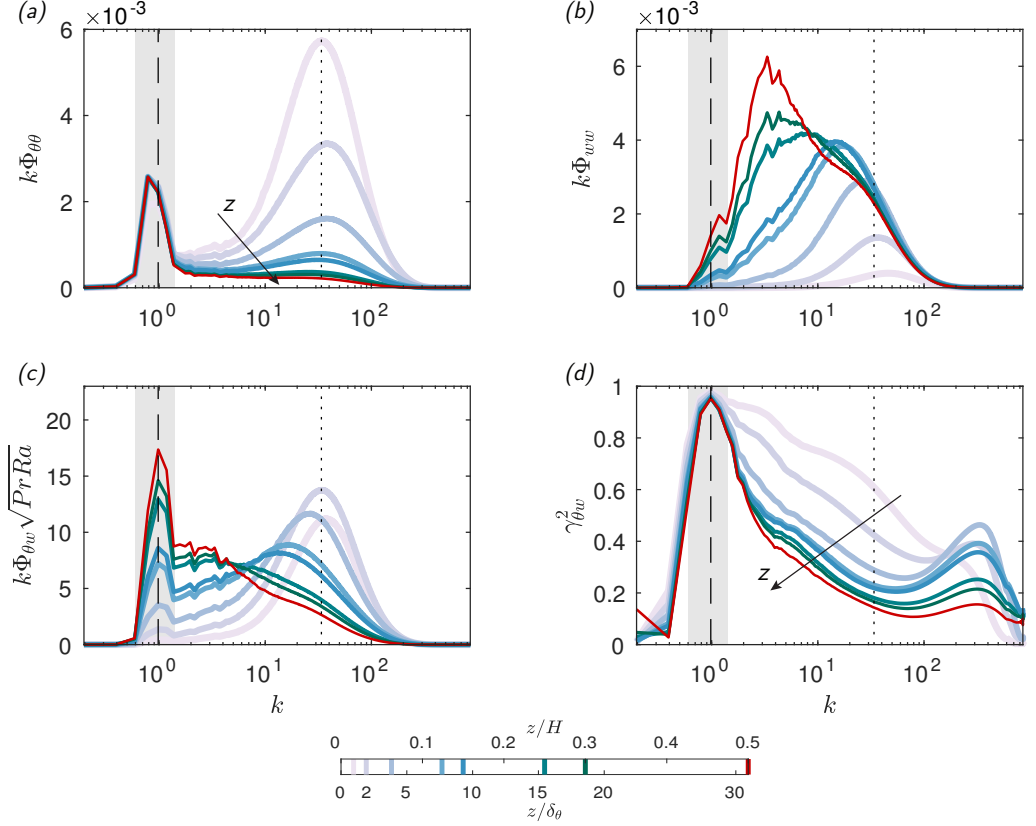


FIGURE 2. Premultiplied temperature (a) and vertical velocity (b) power spectra. The premultiplied co-spectrum $k\Phi_{\theta w}$ (c) is normalized such that it integrates to the turbulent heat flux. (d) Linear coherence spectrum $\gamma_{\theta w}^2$, see eq. (3.2). The dashed and dotted vertical lines indicate $k = 1$ and $k = 34$, respectively. The grey-shaded area marks the approximate range of superstructure scales $k = 1 \pm 0.4$. The results presented here are computed for $Ra = 10^8$. The color of the curves codes the wall distance according to the legend below the figures.

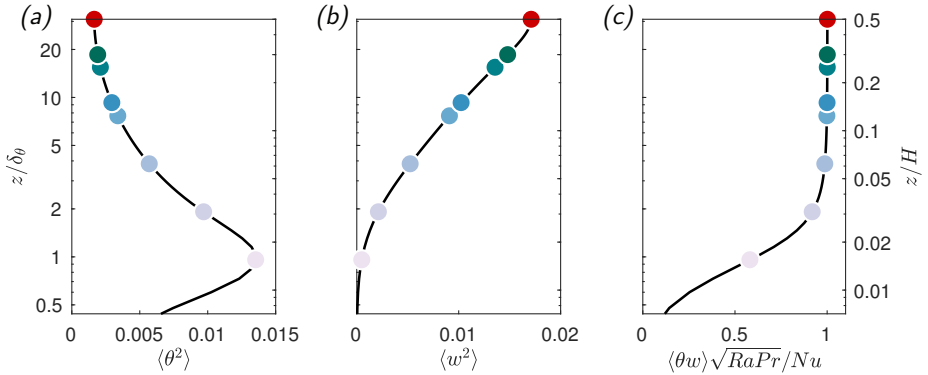


FIGURE 3. Wall-normal temperature (a) and vertical velocity (b) variance profiles for $Ra = 10^8$. Panel (c) shows the corresponding normalized turbulent heat flux. Symbols denote the location of the spectra plotted in figures 2 with corresponding colors.

vertical velocity spectrum $k\Phi_{ww}(z/H = 0.5)$ spans approximately the same range of scales as its temperature counterpart overall. However, its shape is significantly different as it is much more broadband and has a fairly wide peak centered around $k \approx 3.5$. It is important to note, though, that there is significant energy in the $k\Phi_{ww}$ -spectrum at the scales corresponding to the thermal superstructures, which are marked by grey shading in all panels of figure 2. This implies that velocity structures of the same size as the temperature superstructures indeed exist. Yet, their contribution is overshadowed by stronger velocity fluctuations at smaller scales.

More insight into the correlation between the velocity and temperature structures is obtained by analyzing the one-sided co-spectrum $\Phi_{\theta w} = \text{Re}(\langle \mathcal{F}(\theta)\mathcal{F}(w)^* \rangle)$ where $\mathcal{F}(\cdot)$ indicates the Fourier transform in the horizontal plane and $(\cdot)^*$ the complex conjugate. Figure 2c shows that the temperature-velocity co-spectrum $k\Phi_{\theta w}$ at mid-height features a pronounced large-scale peak at $k \approx 1$. This indicates that a correlation exists between the large-scale structures in θ and w . Further, $k\Phi_{\theta w}(z/H = 0.5)$ decreases with increasing k , but scales smaller than the superstructure size nevertheless contribute significantly to the turbulent heat transport. Aside from the degree of correlation between θ and w also their magnitudes factor into the co-spectrum at a given scale. In order to focus on the correlation aspect only, we analyze the linear coherence spectrum

$$\gamma_{\theta w}^2(k) = \frac{|\Phi_{\theta w}(k)|^2}{\Phi_{\theta\theta}(k)\Phi_{ww}(k)}. \quad (3.2)$$

By definition, $0 \leq \gamma_{\theta w}^2 \leq 1$ and the coherence may be interpreted as the square of a scale-dependent correlation coefficient. From figure 2d it is evident that $\gamma_{\theta w}^2 \geq 0.8$ for almost the entire large-scale peak with a maximum value of $\gamma_{\theta w}^2 = 0.95$ at $k = 1$. The coherence quickly drops below $\gamma_{\theta w}^2 = 0.5$ for larger k . This explains why the overall correlation coefficient between θ and w , which is essentially an average over the coherence spectrum, is smaller than 0.5 as reported in Stevens *et al.* (2018).

In order to demonstrate also visually how well the large scales of w and θ are correlated, we present the snapshots from figure 1 again in figure 4, but this time with the small-scale contributions removed. More specifically, we obtain the large-scale fields θ_L and w_L using a spectral low-pass filter where the cut-off wavenumber $k_{cut} = 2.5$ is chosen based on the scale at which $\gamma_{\theta w}^2(z/H = 0.5)$ drops below 0.5. Figure 4 convincingly shows that there is indeed a very good correspondence between patterns at the superstructure scale in temperature and vertical velocity fields, not only in size but also in location.

To summarize, we have shown that patterns corresponding to the thermal superstructures also exist in the vertical velocity. For the vertical velocity, though, the contribution of the superstructures in the $k\Phi_{ww}$ -spectrum is sub-dominant in the sense that it does not result in a spectral peak. This has previously led to the misconception that the *superstructures* in the velocity field are smaller than in the temperature field, whereas it is really the size of the *most energetic structures*, as measured by the spectral peak, that is different. We will revisit the reasons for the different spectral distributions of θ and w in §3.2, but we first discuss the height dependence of the trends discussed so far.

Apart from the results at mid-height, figure 2 also contains data at seven different wall-normal locations that span the full domain down to the thermal boundary layer thickness $\delta_\theta = 1/(2Nu)$. Remarkably, curves at all z -positions collapse around the peak at $k = 1$ for the temperature spectra in figure 2a. This suggests that there is very little evolution of the large-scale thermal structures along the vertical direction. Similarly, also the coherence between θ and w (figure 2d) is almost independent of z at the largest scales. In contrast, there is a pronounced increase in $k\Phi_{ww}$ around $k \approx 1$ with increasing distance away from the wall — a natural consequence of the impermeability condition

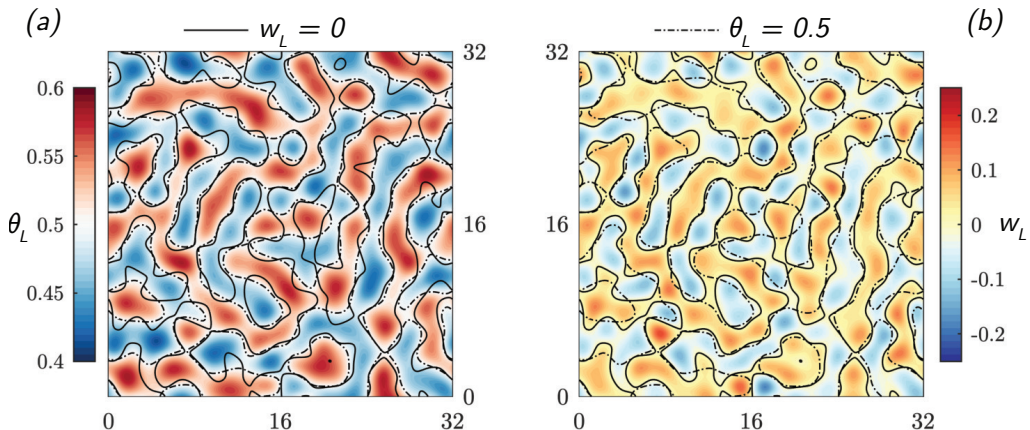


FIGURE 4. Same snapshots of temperature (a) and vertical velocity (b) at mid-height as presented in figure 1, but this time filtered with a spectral low-pass filter with cut-off wavenumber $k_{cut} = 2.5$.

at the wall. It is this increase in $k\Phi_{ww}$ that also drives a growth of the large-scale peak of the co-spectrum as z increases, as shown in figure 2c.

What is striking about the $k\Phi_{\theta\theta}$ spectra (figure 2a) is that at heights of the order of δ_θ there exists a second strong peak in addition to the one caused by the superstructures. This small-scale peak is located at $k \approx 34$ (indicated by the dotted lines in figure 2), which corresponds to a typical small-scale structure size of about $11\delta_\theta$. Upon comparison with figure 3a, it becomes clear that this peak carries the energy that leads to the maximum of $\langle\theta^2\rangle$ at $z = \delta_\theta$. A similar small-scale peak is also observed for $k\Phi_{ww}$ in figure 2b, even though it is located at slightly larger k in this case. For $k\Phi_{ww}$, this peak broadens towards intermediate scales with increasing z and the increase of $\langle w^2\rangle$ with increasing z (see figure 3b) is mostly associated with increasing energy content at intermediate scales $k \approx 10$. It is further interesting to note that the spectral decomposition of $k\Phi_{\theta w}$ shifts from small-scale dominated ($z \lesssim 3\delta_\theta$) over broadband ($0.1H \lesssim z \lesssim 0.2H$) to a maximum at large scales for $z \gtrsim 0.2H$. At the same time, the overall heat transport $\langle\theta w\rangle$ stays approximately constant beyond $z \approx 2\delta_\theta$ (see figure 3c). In connection, these observations appear consistent with the concept of merging plumes as advocated by e.g. Parodi *et al.* (2004), where the structure size increases while the flux remains constant.

3.2. Production of temperature and vertical-velocity fluctuations

In order to uncover the origin of the different spectral distribution of temperature and vertical velocity that became apparent in figure 2a,b, we now study the variance production terms of the respective variance budgets. These production terms are (Deardorff & Willis 1967; Kerr 2001; Togni *et al.* 2015)

$$S_\theta = -2\langle\theta w\rangle \frac{d\Theta}{dz} \quad (3.3)$$

for $\langle\theta^2\rangle$ and

$$S_w = \langle\theta w\rangle \quad (3.4)$$

for $\langle w^2\rangle$. A trivial but nevertheless important implication that arises from comparing (3.3) and (3.4) is that $\langle\theta w\rangle$ generates w -variance *directly*, while temperature variance is only produced in the presence of a mean gradient $d\Theta/dz$. Consequently, $S_\theta > 0$ is

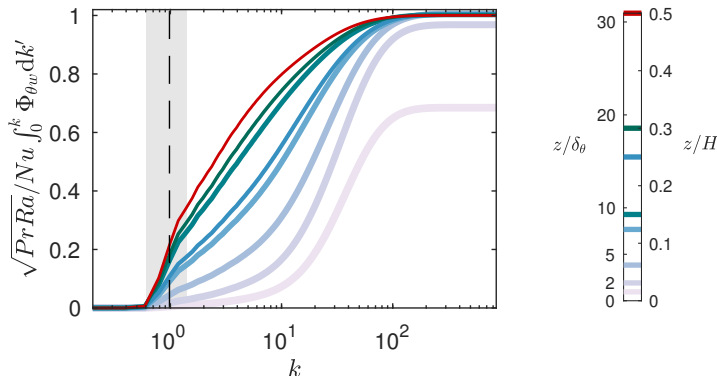


FIGURE 5. Cumulative co-spectrum $\int_0^k \Phi_{\theta w} dk'$ for $Ra = 10^8$. The corresponding co-spectra $k\Phi_{\theta w}$ are shown in figure 2c.

restricted to the thermal boundary layer ($z \lesssim \delta_\theta$) since a significant mean temperature gradient exists only there. This close to the wall $\langle \theta w \rangle$ is predominantly a small-scale quantity as evidenced by $k\Phi_{\theta w}(z = \delta_\theta)$ in figure 2c, such that S_θ is localized not only in space but also in scale. On the contrary, $\langle \theta w \rangle$ is almost independent of z outside of the thermal boundary layer, see figure 3c. Hence, also S_w is widely distributed across the bulk of the flow. To better understand the spectral distribution of S_w , we present the data from figure 2c in cumulative form in figure 5. This figure reveals that even at $z/H = 0.5$ the large-scale peak of $\Phi_{\theta w}$ only contributes about 30% of the total flux $\langle \theta w \rangle$. In the central region of the flow the bulk of the $\langle w^2 \rangle$ production occurs at intermediate scales (say $2 \lesssim k \lesssim 10$). This coincides with the scales at which $k\Phi_{ww}$ peaks at these wall distances, see figure 2b. This further explains why the superstructure contribution is not reflected as a spectral peak in the $k\Phi_{ww}$ spectrum.

While the analysis of the production terms provides essential insight into the reasons for the different spectral decomposition of $\langle \theta^2 \rangle$ and $\langle w^2 \rangle$, other aspects cannot be addressed on this basis alone. Specifically, understanding the apparently very efficient organization of small-scale temperature fluctuations into thermal superstructures requires the analysis of inter-scale energy transfer. Such an inverse, i.e., from the small-scales to larger scales, energy transfer, is indeed observed in RBC e.g. by Togni *et al.* (2015) for both velocity and temperature in RBC at moderate aspect ratio.

3.3. Wall-normal coherence of superstructures

So far, we have only considered the correlation between vertical velocity and temperature at a given wall-normal location. Another important aspect is the wall-normal coherence of superstructures. There exists anecdotal evidence from comparing snapshots at different heights that an imprint of the large-scale structures is visible in the boundary layers (Stevens *et al.* 2018; Pandey *et al.* 2018). To corroborate these findings in a more systematic and quantitative manner, we again turn to the linear coherence spectrum. However, this time we do not evaluate coherence between different fields, but now we evaluate the same fields at different heights z and z_R according to

$$\gamma_{\psi\psi}^2(z_R; z, k) = \frac{|\langle \mathcal{F}(\psi(z_R)) \mathcal{F}(\psi(z))^* \rangle|^2}{\Phi_{\psi\psi}(z_R, k) \Phi_{\psi\psi}(z, k)}. \quad (3.5)$$

We fix the reference height at $z_R = \delta_\theta$. Consequently, $\gamma_{\psi\psi}^2(z_R = \delta_\theta; z, k)$ is a measure of how correlated structures in field ψ at scale k and height z are with fluctuations of the same scale at boundary layer height of the same field. Results are presented for

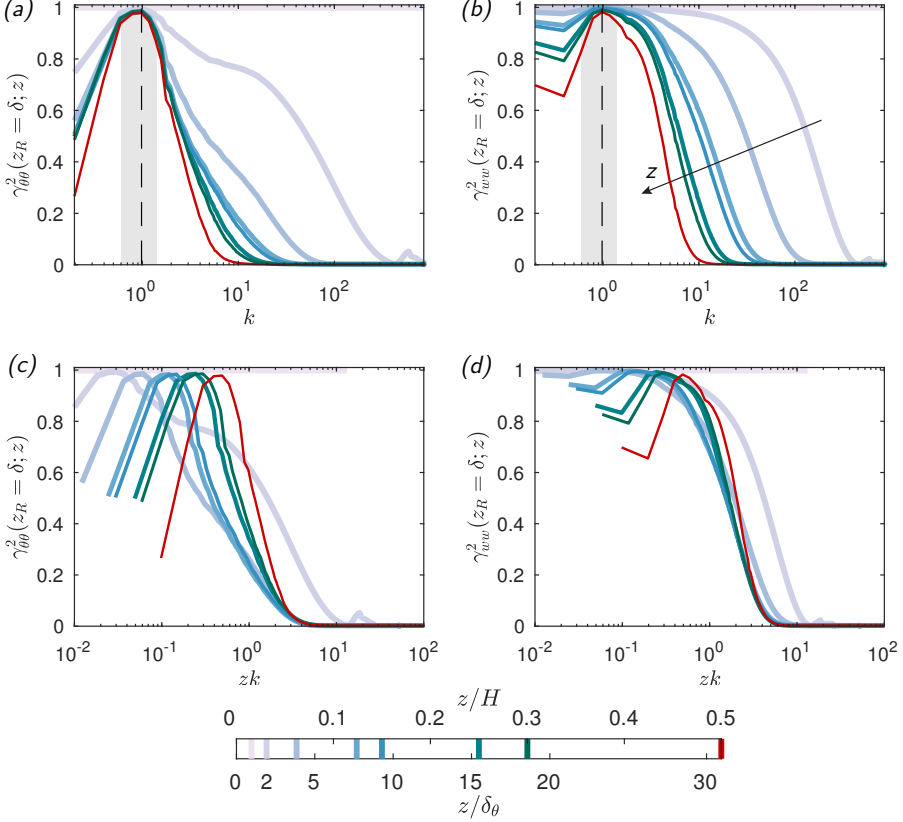


FIGURE 6. Spatial coherence spectra of (a) temperature and (b) vertical velocity with the reference plane at $z_R = \delta_\theta$. The data from (a) and (b) is plotted again in (c) and (d), respectively, as a function of zk instead of k . All results shown are for $Ra = 10^8$.

temperature and vertical velocity in figures 6a and 6b, respectively. By definition, the result at $z = \delta_\theta$ is the correlation with the reference itself and therefore $\gamma_{\psi\psi}^2(z_R = \delta_\theta; \delta_\theta, k) = 1$ trivially. In the superstructure peak ($k = 1 \pm 0.4$, marked by grey shading in the figure) $\gamma_{\psi\psi}^2(z_R = \delta_\theta; z, k)$ is close to one, even at mid-height. This holds for both temperature and vertical velocity and implies a very strong degree of spatial coherence for the largest structures in both fields. Differences between θ and w only occur at smaller scales. Beyond $z = 2\delta_\theta$ the spatial coherence of θ decreases very quickly as a function of k , but has a limited z -dependence. In contrast, curves for γ_{ww}^2 in figure 6b show significant variation with z with the decline occurring at progressively smaller k with increasing z . Apart from quantifying the correlation, $\gamma_{\psi\psi}^2(z_R = \delta_\theta)$ also provides information about the self-similarity of structures that are connected or ‘attached’ to the thermal boundary layer. This is of interest since previous authors (e.g. He *et al.* 2014; Ahlers *et al.* 2014) have referred to the attached-eddy framework (Townsend 1976; Perry & Chong 1982; Marusic & Monty 2019), which assumes the existence of self-similar wall-attached structures, in the interpretation of their results. For the coherence spectrum, self-similarity implies that curves of $\gamma_{\psi\psi}^2(z_R = \delta_\theta)$ should collapse if plotted against zk , that is if the scale is normalized by the distance from the wall (see Baars *et al.* 2017; Krug *et al.* 2019). We test this for temperature and vertical velocity in figures 6c,d. Clearly, self-similarity is not observed for the temperature (figure 6c). However, figure 6d shows that the data for w indeed collapse to a reasonable degree for $3\delta_\theta < z < 0.3H$. To check if self-similarity

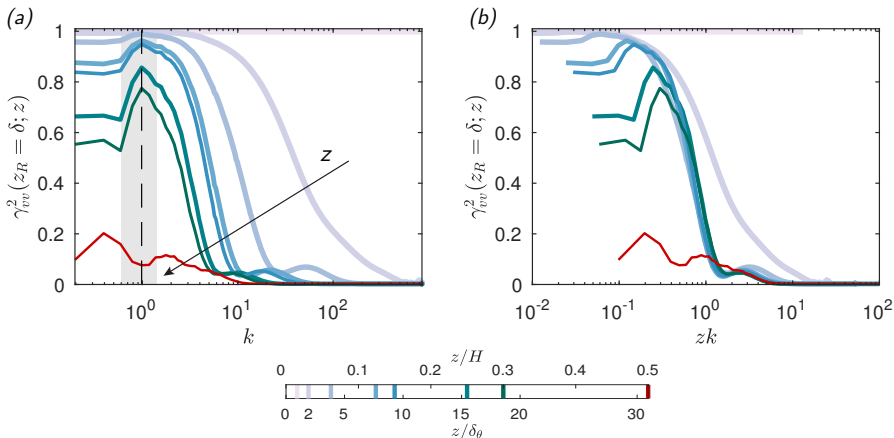


FIGURE 7. Spatial coherence spectra of horizontal velocity v as a function of (a) k and (b) zk . The reference height is $z_R = \delta_\theta$ and $Ra = 10^8$.

scaling in this range is a property of the velocity field in generally, we additionally present results for $\gamma_{vv}^2(z_R = \delta_\theta)$, where v is the horizontal velocity component, in figure 7. The vertical coherence of v also exhibits the same superstructure peak as observed for the other quantities (figure 7a). Only its magnitude decreases with increasing z and is close to zero at mid-height. This is consistent with the roll structures not having a horizontal component at $z/H \approx 0.5$ and also the spectral energy $\Phi_{vv}(k = 1 \pm 0.4)$ (not shown) is minimal there. As figure 7b shows, $\gamma_{vv}^2(z_R = \delta_\theta)$ displays the same collapse when plotted versus zk and in the same range of z as previously observed for w . This means that for the velocity fields in a significant part of the domain (at least $3\delta_\theta \lesssim z \lesssim 0.3H$) structures attached to the boundary layer display self-similar behavior. The same trends are observed at different Ra but are not shown here for brevity.

3.4. Rayleigh number trends

As a final point, we study the Ra number dependence of the properties discussed in §3.1. To this end, we present results for $\gamma_{\theta w}^2$ evaluated at mid-height for $10^5 \leq Ra \leq 10^9$ in figure 8a. The magnitude and the shape of the large-scale peak are nearly independent of Ra . However, the peak location shifts towards smaller k with increasing Ra . The corresponding increase in the large-scale structure is quantified in figure 8b, where the triangles indicate the structure size ($\hat{l} = 2\pi/\hat{k}$) corresponding to the peak in the coherence. Here, the peak location \hat{k} is obtained from fitting a parabola to three points centered around the peak of $\gamma_{\theta w}^2$ and the results are also listed in table 1. Evidently, \hat{l} is significantly larger than the wavelength of the structure at the onset of convection, which is ≈ 2 (e.g. Drazin & Reid 2004). Additionally, length scales corresponding to the spectral peak in $\Phi_{\theta\theta}$ (circles), Φ_{ww} (filled squares), and $k\Phi_{ww}$ (open squares) are included in figure 8b and the corresponding spectra are shown in panels (c,d) of the same figure. The spectral peak from the temperature spectrum corresponds to slightly larger length scales compared to the results based on $\gamma_{\theta w}^2$, but the differences are quite small. Due to its broadband nature, the spectral peaks for the vertical velocity are found at a different location in the regular and premultiplied spectra. The maximum of Φ_{ww} only agrees with the results based on coherence and temperature at $Ra = 10^5$. For higher Ra fluctuations at intermediate length scales dominate the velocity spectrum. Therefore, the use of the

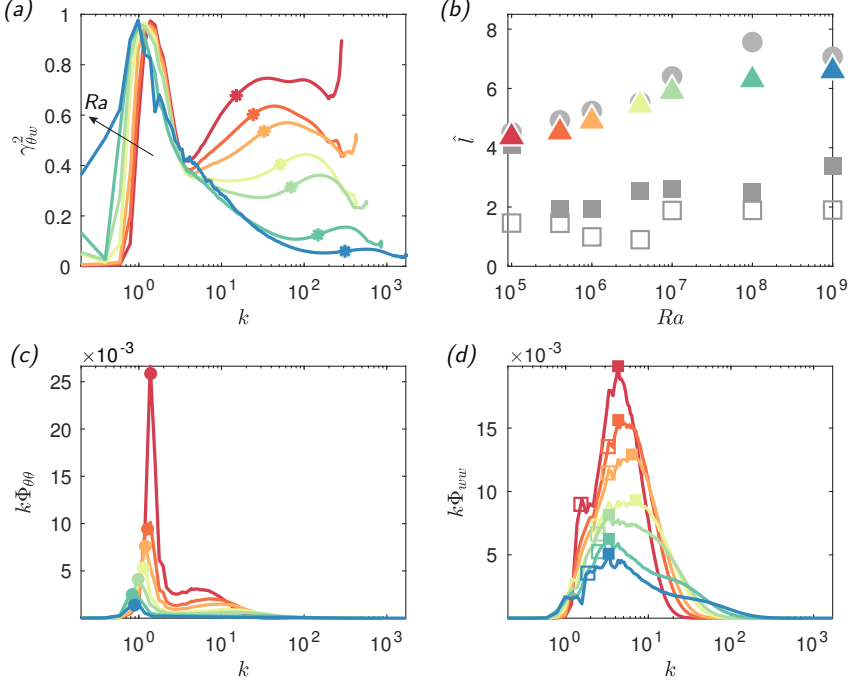


FIGURE 8. (a) Coherence spectrum at mid-height for $10^5 \leq Ra \leq 10^9$; see panel (b) for the color-code. Stars indicate the wavenumber corresponding to 10η at the respective Ra . (b) Wavelength \hat{l} of the spectral peaks of $\gamma_{\theta w}^2$ (triangles), $\Phi_{\theta\theta}$ (circles), Φ_{ww} (filled squares) and $k\Phi_{ww}$ (open squares). The corresponding spectra $k\Phi_{\theta\theta}$ and $k\Phi_{ww}$ are shown in panels (c) and (d) with symbols marking the peak locations as described for (b).

velocity spectra leads to significantly lower estimates for \hat{l} than the temperature spectra at higher Ra , as mentioned in §3.1.

The concept of a convection roll, i.e. a thermally driven velocity structure, suggests to define the superstructure size in RBC as the scale where the correlation between temperature and velocity fields is maximum. We therefore argue that conceptually the most straightforward way to define the superstructure size is via the coherence spectrum. It should be noted that the coherence peak is not necessarily coincident with the peak of the co-spectrum due to the different distributions of $\Phi_{\theta\theta}$ and Φ_{ww} . In practice, however, the peaks of $\gamma_{\theta w}^2$ and $\Phi_{\theta w}$ coincide within measurement accuracy for the cases presented here. This seems to be a consequence of the sharp drop-off of $\gamma_{\theta w}^2$ with increasing k , but the situation may change e.g. for different Pr numbers. The peaks of the Φ_{ww} and the $k\Phi_{ww}$ spectra are not a suitable indicators for superstructure size.

As an aside, we discuss the increase of $\gamma_{\theta w}^2$ that is seen to occur at high k in figure 8a. This increase at small-scales occurs for lower values of k and is stronger for the lower Ra . A comparison with figure 8c,d reveals that there is only minimal energy at these small scales. These observations are consistent with the notion that the higher values of $\gamma_{\theta w}^2$ mark the transition to a viscous dominated regime. In the viscous regime, the correlation between θ and w is high because the balance is predominantly between buoyancy and viscous forces. To lend support to this understanding, we added the length scale 10η as a reference scale for the viscous regime in the figure. Here, $\eta = (\nu^3/\langle\varepsilon\rangle_V)^{1/4}$ is the Kolmogorov length-scale and $\langle\varepsilon\rangle_V$ is the volume-averaged dissipation rate obtained from the identity $\langle\varepsilon\rangle_V = (Nu - 1)/\sqrt{RaPr}$. It is seen in figure 8a that the scale at which the

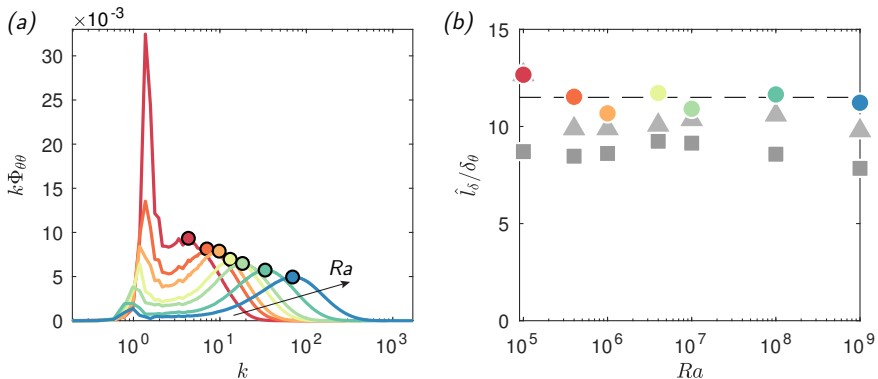


FIGURE 9. (a) Premultiplied temperature power spectra $k\Phi_{\theta\theta}$ at $z = \delta_\theta$ for $10^5 \leq Ra \leq 10^9$. Symbols mark the location of the small-scale peak determined as the maximum of $k\Phi_{\theta\theta}(k)$ for $k > 2$. Note that at the lower Ra , this peak does not correspond to a global maximum of $k\Phi_{\theta\theta}$. (b) Length scale \hat{l}_δ associated with the small-scale peak of $k\Phi_{\theta\theta}$ (circles), $k\Phi_{ww}$ (squares) and $k\Phi_{\theta w}$ (triangles) normalized with the thermal boundary layer thickness δ_θ . The dashed line is at 11.5 for reference.

high-wavenumber increase of $\gamma_{\theta w}^2$ occurs roughly coincides with 10η at all Ra , just as expected from the above.

The Ra dependence of the near-wall characteristics of the temperature field are displayed in figure 9 in which $k\Phi_{\theta\theta}$ is plotted at $z = \delta_\theta$ for each Ra . This figure shows that the small-scale peak contributes an increasingly larger part of the total energy with increasing Ra . At the same time, the scale separation between the small-scales and the large-scale superstructures increases with increasing thermal driving. We define the length scale of the small-scale structures as $\hat{l}_\delta = 2\pi/\hat{k}_\delta$, where \hat{k}_δ is the location of the high- k peak. Figure 9b shows that \hat{l}_δ is approximately constant for $10^5 \leq Ra \leq 10^9$, when normalized with the boundary layer thickness δ_θ . The magnitude of the ratio $\hat{l}_\delta/\delta_\theta$ differs slightly depending on the quantity considered. The most energetic small-scale structures for the temperature are about $11.5\delta_\theta$, for w it is about $8.5\delta_\theta$, and $k\Phi_{\theta w}$ peaks at about $10\delta_\theta$.

4. Conclusion

Contrary to prior speculations (Stevens *et al.* 2018; Pandey *et al.* 2018), we found that superstructures of approximately *the same size* exist in the fields of temperature and vertical velocity in large-aspect ratio Rayleigh-Bénard flow. These result in a very significant large-scale peak in the linear coherence spectrum of θ and w that signifies almost perfect correlation at those length scales. Unlike it is the case for θ , we find that the superstructures in w do not correspond to a spectral peak in the power spectrum of w . This difference has previously led to the above-mentioned confusion regarding potentially different sizes of the largest structures in θ and w . The fact that the most energetic motions, as measured by the peak in the spectra, occur at intermediate scales for w , but at the superstructure scale for θ , can be explained by differences in the production terms of the respective variance budgets. In particular, temperature production is confined to the boundary layer and small-scales, while buoyancy forcing acts at intermediate scales and throughout the entire bulk of the flow. Furthermore, we find that the superstructure scale increases with Ra for $10^5 \leq Ra \leq 10^9$, i.e. the full range investigated here, when the structure size is based on the coherence spectrum as suggested. It should be noted that

integral length scales of temperature and turbulent kinetic energy as used in Stevens *et al.* (2018) do not accurately capture this growth, which shows the importance of selecting the appropriate metric to quantify superstructures in RBC.

In agreement with previous observations of superstructure footprints in the boundary layer region, we find an almost perfect spatial correlation of the superstructure scales from the boundary-layer height δ_θ up to mid-height, for both θ and w . Also, the temperature spectra, as well as $\gamma_{\theta w}^2$, are seen to collapse at different heights. Hence, there is no noticeable dependence of the superstructure scale on z , effectively ruling out a significant growth of the thermal structures due to horizontal transport while they are travelling upward as was suggested by Pandey *et al.* (2018). The decrease of spatial correlation (quantified by the linear coherence spectrum) at intermediate scales when increasing the distance to the reference height δ_θ is observed to follow a self-similar trend for w and the horizontal component v , but not for θ . The reason for this difference remains unclear but warrants further investigation.

Moreover, we find that the energy distribution of the temperature field is bimodal. Besides the z -independent large-scale contribution of the superstructures, premultiplied spectra reveal the existence of a pronounced small-scale peak at boundary-layer height. The two peaks are separated by a spectral gap that increases with Ra , which is also visible in the co-spectra of θ and w . However, $k\Phi_{ww}$ displays a small-scale peak only near the wall and is broadband otherwise. For the temperature fluctuations, the small-scale peak carries the energy that leads to the maximum of $\langle\theta^2\rangle$ at $z = \delta_\theta$ (see e.g. Wang *et al.* 2016). The length scale of the associated structures is approximately $l_\delta \approx 10\delta_\theta$. It is interesting to note that the situation described here has a close resemblance to findings in turbulent boundary layers. There an ‘inner peak’ is observed that is fixed at 15 viscous units (l_{visc}) away from the wall and with typical streamwise length scales of about $1000l_{visc}$ (Hutchins & Marusic 2007b). The scale separation between the ‘inner peak’ and the large-scale structures is, however, significantly stronger in RBC. This appears to suggest distinctly different processes, as was already pointed out in Pandey *et al.* (2018) in a different context, and raises questions about their interaction. A better understanding of these aspects will be very insightful for modelling approaches.

The authors acknowledge stimulating discussions with Woutijn Baars. This work is supported by the Twente Max-Planck Center, the German Science Foundation (DFG) via program SSP 1881, and the ERC (the European Research Council) Starting Grant No. 804283 UltimateRB. The authors gratefully acknowledge the Gauss Centre for Supercomputing e.V. (www.gauss-centre.eu) for funding this project by providing computing time on the GCS Supercomputer SuperMUC-NG at Leibniz Supercomputing Centre (www.lrz.de). Part of the work was carried out on the national e-infrastructure of SURFsara, a subsidiary of SURF cooperation, the collaborative ICT organization for Dutch education and research.

REFERENCES

- AHLERS, G., BODENSCHATZ, E. & HE, X. 2014 Logarithmic temperature profiles of turbulent Rayleigh-Bénard convection in the classical and ultimate state for a Prandtl number of 0.8. *J. Fluid Mech.* **758**, 436–467.
- AHLERS, G., GROSSMANN, S. & LOHSE, D. 2009 Heat transfer and large scale dynamics in turbulent Rayleigh-Bénard convection. *Rev. Mod. Phys.* **81** (2), 503–537.
- BAARS, W. J., HUTCHINS, N. & MARUSIC, I. 2017 Self-similarity of wall-attached turbulence in boundary layers. *J. Fluid Mech.* **823** (R2).

- BAILON-CUBA, J., EMRAN, M. S. & SCHUMACHER, J. 2010 Aspect ratio dependence of heat transfer and large-scale flow in turbulent convection. *J. Fluid Mech.* **655**, 152–173.
- CHILLÀ, F. & SCHUMACHER, J. 2012 New perspectives in turbulent Rayleigh-Bénard convection. *Eur. Phys. J. E* **35** (7), 58.
- CIERPKA, C., KÄSTNER, C., RESAGK, C. & SCHUMACHER, J. 2019 On the challenges for reliable measurements of convection in large aspect ratio Rayleigh-Bénard cells in air and sulfur-hexafluoride. *Exp. Therm. Fluid Sci.* p. 109841.
- DEARDORFF, J. W. & WILLIS, G. E. 1967 Investigation of turbulent thermal convection between horizontal plates. *J. Fluid Mech.* **28** (4), 675–704.
- DRAZIN, P. G. & REID, W. H. 2004 *Hydrodynamic stability*. Cambridge Univ. Press.
- DU PUIS, R., RESAGK, C. & THESS, A. 2013 Thermal boundary layers in turbulent Rayleigh-Bénard convection at aspect ratios between 1 and 9. *New J. Phys.* **15** (1), 013040.
- EMRAN, M. S. & SCHUMACHER, J. 2015 Large-scale mean patterns in turbulent convection. *J. Fluid Mech.* **776**, 96–108.
- FITZJARRALD, D. E. 1976 An experimental study of turbulent convection in air. *J. Fluid Mech.* **73** (4), 693–719.
- GREEN, G., VLAYKOV, D. G., MELLADO, J. P. & WILCZEK, M. 2019 Resolved energy budget of superstructures in Rayleigh-Bénard convection. *arXiv preprint arXiv:1905.10278*.
- HARTLEP, T., TILGNER, A. & BUSSE, F. H. 2003 Large scale structures in Rayleigh-Bénard convection at high Rayleigh numbers. *Phys. Rev. Lett.* **91** (6), 064501.
- HARTLEP, T., TILGNER, A. & BUSSE, F. H. 2005 Transition to turbulent convection in a fluid layer heated from below at moderate aspect ratio. *J. Fluid Mech.* **544**, 309–322.
- HE, X., VAN GILS, D. P. M., BODENSCHATZ, E. & AHLERS, G. 2014 Logarithmic spatial variations and universal f^{-1} power spectra of temperature fluctuations in turbulent Rayleigh-Bénard convection. *Phys. Rev. Lett.* **112** (17), 174501.
- HOGG, J. & AHLERS, G. 2013 Reynolds-number measurements for low-Prandtl-number turbulent convection of large-aspect-ratio samples. *J. Fluid Mech.* **725**, 664–680.
- HUISMAN, S. G., VAN DER VEEN, R. C., SUN, C. & LOHSE, D. 2014 Multiple states in highly turbulent Taylor-Couette flow. *Nat. Commun.* **5**, 3820.
- HUTCHINS, N. & MARUSIC, I. 2007a Evidence of very long meandering features in the logarithmic region of turbulent boundary layers. *J. Fluid Mech.* **579**, 1–28.
- HUTCHINS, N. & MARUSIC, I. 2007b Large-scale influences in near-wall turbulence. *Philos. Trans. Royal Soc. A* **365** (1852), 647–664.
- KERR, R. M. 2001 Energy budget in Rayleigh-Bénard convection. *Phys. Rev. Lett.* **87** (24), 244502.
- KRUG, D., BAARS, W. J., HUTCHINS, N. & MARUSIC, I. 2019 Vertical coherence of turbulence in the atmospheric surface layer: Connecting the hypotheses of Townsend and Davenport. *Bound.-Layer Meteorol.* **172** (2), 199–214.
- LEE, M. & MOSER, R. D. 2018 Extreme-scale motions in turbulent plane Couette flows. *J. Fluid Mech.* **842**, 128–145.
- LOHSE, D. & XIA, K.-Q. 2010 Small-scale properties of turbulent Rayleigh-Bénard convection. *Annu. Rev. Fluid Mech.* **42**, 335–364.
- MARUSIC, I. & MONTY, J. P. 2019 Attached eddy model of wall turbulence. *Annu. Rev. Fluid Mech.* **51**, 49–74.
- MORRIS, S. W., BODENSCHATZ, E., CANNELL, D. S. & AHLERS, G. 1993 Spiral defect chaos in large aspect ratio Rayleigh-Bénard convection. *Phys. Rev. Lett.* **71** (13), 2026.
- PANDEY, A., SCHEEL, J. D. & SCHUMACHER, J. 2018 Turbulent superstructures in Rayleigh-Bénard convection. *Nat. Commun.* **9** (1), 2118.
- PARODI, A., VON HARDENBERG, J., PASSONI, G., PROVENZALE, A. & SPIEGEL, E. A. 2004 Clustering of plumes in turbulent convection. *Phys. Rev. Lett.* **92** (19), 194503.
- PERRY, A. E. & CHONG, M. S. 1982 On the mechanism of wall turbulence. *J. Fluid Mech.* **119**, 173–217.
- VAN DER POEL, E. P., OSTILLA-MÓNICO, R., DONNERS, J. & VERZICCO, R. 2015 A pencil distributed finite difference code for strongly turbulent wall-bounded flows. *Computers & Fluids* **116**, 10–16.
- SAKIEVICH, P. J., PEET, Y. T. & ADRIAN, R. J. 2016 Large-scale thermal motions of turbulent

- Rayleigh-Bénard convection in a wide aspect-ratio cylindrical domain. *Int. J. Heat Mass Transf.* **61**, 183–196.
- SHISHKINA, O., STEVENS, R. J. A. M., GROSSMANN, S. & LOHSE, D. 2010 Boundary layer structure in turbulent thermal convection and its consequences for the required numerical resolution. *New J. Phys.* **12**, 075022.
- SHISHKINA, O. & WAGNER, C. 2005 A fourth order accurate finite volume scheme for numerical simulations of turbulent Rayleigh-Bénard convection in cylindrical containers. *C. R. Mecanique* **333**, 17–28.
- SHISHKINA, O. & WAGNER, C. 2006 Analysis of thermal dissipation rates in turbulent Rayleigh-Bénard convection. *J. Fluid Mech.* **546**, 51–60.
- SHISHKINA, O. & WAGNER, C. 2007 Local heat fluxes in turbulent Rayleigh-Bénard convection. *Phys Fluids* **19**, 085107.
- STEVENS, R. J. A. M., BLASS, A., ZHU, X., VERZICCO, R. & LOHSE, D. 2018 Turbulent thermal superstructures in Rayleigh-Bénard convection. *Phys. Rev. Fluids* **3** (4), 041501.
- STEVENS, R. J. A. M., LOHSE, D. & VERZICCO, R. 2011 Prandtl and Rayleigh number dependence of heat transport in high Rayleigh number thermal convection. *J. Fluid Mech.* **688**, 31–43.
- STEVENS, R. J. A. M., VERZICCO, R. & LOHSE, D. 2010 Radial boundary layer structure and Nusselt number in Rayleigh-Bénard convection. *J. Fluid Mech.* **643**, 495–507.
- SUN, C., REN, L.-Y., SONG, H. & XIA, K.-Q. 2005*a* Heat transport by turbulent Rayleigh-Bénard convection in 1 m diameter cylindrical cells of widely varying aspect ratio. *J. Fluid Mech.* **542**, 165–174.
- SUN, C., REN, L.-Y., SONG, H. & XIA, K.-Q. 2005*b* Heat transport by turbulent Rayleigh-Bénard convection in 1m diameter cylindrical cells of widely varying aspect ratio. *J. Fluid Mech.* **542**, 165–174.
- TOGNI, R., CIMARELLI, A. & DE ANGELIS, E. 2015 Physical and scale-by-scale analysis of Rayleigh-Bénard convection. *J. Fluid Mech.* **782**, 380–404.
- TOWNSEND, A. A. 1976 *The Structure of Turbulent Shear Flow*. Cambridge Univ. Press.
- VERZICCO, R. & ORLANDI, P. 1996 A finite-difference scheme for three-dimensional incompressible flow in cylindrical coordinates. *J. Comput. Phys.* **123**, 402–413.
- VON HARDENBERG, J., PARODI, A., PASSONI, G., PROVENZALE, A. & SPIEGEL, E. A. 2008 Large-scale patterns in Rayleigh-Bénard convection. *Physics Letters A* **372** (13), 2223–2229.
- WANG, Y., HE, X. & TONG, P. 2016 Boundary layer fluctuations and their effects on mean and variance temperature profiles in turbulent Rayleigh-Bénard convection. *Phys. Rev. Fluids* **1** (8), 082301.
- YOUNG, G. S., KRISTOVICH, D. A. R., HJELMFELT, M. R. & FOSTER, R. C. 2002 Rolls, streets, waves, and more: A review of quasi-two-dimensional structures in the atmospheric boundary layer. *Bull. Am. Meteorol. Soc.* **83** (7), 997–1002.
- ZHOU, Q., LIU, B.-F., LI, C.-M. & ZHONG, B.-C. 2012 Aspect ratio dependence of heat transport by turbulent Rayleigh-Bénard convection in rectangular cells. *J. Fluid Mech.* **710**, 260–276.
- ZHU, X., PHILLIPS, E., ARZA, V. S., DONNERS, J., RUETSCH, G., ROMERO, J., OSTILLA-MÓNICO, R., YANG, Y., LOHSE, D., VERZICCO, R., FATICA, M. & STEVENS, R. J. A. M. 2018 AFiD-GPU: a versatile Navier-Stokes solver for wall-bounded turbulent flows on GPU clusters. *Comput. Phys. Commun.* **229**, 199–210.